Space Weather

RESEARCH ARTICLE
10.1029/2021SW002891

Development of the Storm-Induced Ionospheric Irregularities at Equatorial and Middle Latitudes During the 25–26 August 2018 Geomagnetic Storm

Iurii Cherniak[1,2] **and Irina Zakharenkova**[1,2]

[1]COSMIC Program Office, University Corporation for Atmospheric Research, Boulder, CO, USA, [2]Space Radio-Diagnostic Research Center, University of Warmia and Mazury, Olsztyn, Poland

Key Points:

- Geomagnetic storm in solar minimum initiated development of equatorial ionospheric irregularities of large latitudinal extent upto 25° magnetic latitude (MLAT)
- Plasma depletions of equatorial origin transported in northwestward direction across midlatitudes toward auroral zone
- Atypical ionospheric irregularities moving toward higher latitudes cause rare spread-F echoes at a midlatitude ionosonde (42° MLAT)

Correspondence to:
I. Cherniak,
tcherniak@ukr.net

Citation:
Cherniak, I., & Zakharenkova, I. (2022). Development of the storm-induced ionospheric irregularities at equatorial and middle latitudes during the 25–26 August 2018 geomagnetic storm. *Space Weather*, *20*, e2021SW002891. https://doi.org/10.1029/2021SW002891

Received 23 AUG 2021
Accepted 2 JAN 2022

Author Contributions:
Conceptualization: Iurii Cherniak
Data curation: Iurii Cherniak, Irina Zakharenkova
Formal analysis: Iurii Cherniak, Irina Zakharenkova
Investigation: Iurii Cherniak
Methodology: Iurii Cherniak
Resources: Irina Zakharenkova
Software: Irina Zakharenkova
Validation: Irina Zakharenkova
Visualization: Irina Zakharenkova
Writing – original draft: Iurii Cherniak
Writing – review & editing: Iurii Cherniak

Abstract Can geomagnetic storms during low solar activity trigger formation of extreme equatorial plasma bubbles (EPBs) that affect low and midlatitudes? We analyzed the ionospheric response to the 25–26 August 2018 geomagnetic storm and revealed formation of intense ionospheric plasma irregularities over broad latitudinal ranges from equatorial toward middle latitudes in the American and Pacific sectors. Storm-induced penetration electric fields created favorable conditions for strong fountain effect uplifted the equatorial ionosphere, enhancement of the equatorial ionization anomaly (EIA), and postsunset EPBs generation. We found two patterns of equatorial ionospheric irregularities expansion toward low and middle latitudes: (a) storm-induced EPBs developed over a large latitudinal extent between widely spread EIA crests, (b) narrow channel of the ionospheric irregularities stretched away from the EPB location toward the auroral zone in the northwestward direction. The EPBs latitudinal extent largely exceeded climatological-based expectations for solar minimum conditions; EPBs reached atypically high latitudes (20°–25° magnetic latitude [MLAT]) in the Pacific Ocean sector. The poleward-streaming plasma density depletions were registered along the western coast of North America. The ionospheric irregularities transported in the northwestward direction toward midlatitudes reaching as high as 40°–45° MLAT. The passage of these ionospheric irregularities coincided with the spread-F conditions recorded at a midlatitude ionosonde (42° MLAT)—rather atypical phenomenon for midlatitudes. It is suggested that enhanced westward drifts associated with prompt penetration and Sub Auroral Polarization Stream electric fields can support the northwestward plasma transportation.

Plain Language Summary The 25–26 August 2018 geomagnetic storm occurred at the background of very low solar activity. For this storm, we registered occurrence of very intense ionospheric plasma irregularities developed in the equatorial region and expanded toward much higher latitudes. We revealed that the storm-induced equatorial ionospheric irregularities expended toward middle latitudes in two ways: (a) storm-induced plasma bubbles initially developed with a large latitudinal extent in the uplifted equatorial ionosphere, and (b) poleward part of the largely expanded can be involved into transportation in the northwestward across midlatitudes. The ionospheric irregularities were transported in the northwestward direction toward middle latitudes reaching as high as 40°–45° magnetic latitude (MLAT). The passage of these ionospheric irregularities coincided with the spread-F conditions recorded at a midlatitude ionosonde (42° MLAT)—it is rather atypical phenomenon for midlatitudes, such scattered echoes are typically observed at nighttime at ionosondes located in the equatorial region. It is suggested that enhanced westward drifts associated with strong storm-time electric fields can support the northwestward plasma transportation.

1. Introduction

The 25–26 August 2018 space weather event was classified as the third largest geomagnetic storm of the twenty fourth solar cycle (in terms of the Dst minimum excursion) after the March 2015 and June 2015 geomagnetic storms. The slowly moving coronal mass ejection (CME) occurring on 20 August 2018 was expected to cause a minor geomagnetic activity only, but surprisingly it turned into a strong geomagnetic storm at the very end of the twenty fourth solar cycle. The space weather events of such intensity occurring during the solar minimum period and at the background of the very low ionospheric density can result in a strong ionosphere–thermosphere response. Several recent papers were devoted to the investigation of the positive and negative ionospheric storm effects on the ionospheric density distribution over the globe (Astafyeva et al., 2020; Mansilla & Zossi, 2020;

Younas et al., 2020), as well as regional effects in Asia (Lissa et al., 2020) and over Brazil (Spogli et al., 2021), and reported interhemispheric asymmetries of the ionospheric response during this event.

Another crucial aspect of the Earth's ionosphere response is generation of different scale ionospheric irregularities driven by geomagnetic storm development. Strong geomagnetic storms lead to an occurrence of intense high-latitude ionospheric irregularities due to auroral particle precipitation and high-latitude ionospheric electric field (Keskinen & Ossakow, 1983; Tsunoda, 1988). The equatorward edge of the auroral irregularities zone locates just poleward of the main ionospheric trough (MIT). There also exists a subauroral region of ionospheric irregularities that lies equatorward of the MIT minimum. In particular, there are irregularities in the subauroral region near the evening terminator, called dusk scatter event (DUSEfirst reported by Ruohoniemi et al., 1988), whose source region collocated with the MIT minimum (Hosokawa & Nishitani, 2010) and these irregularities are frequently observed after sunset by Super Dual Auroral Radar Network (SuperDARN) coherent backscatter radars (Nishitani et al., 2019). During storms, one of the most expected ionospheric effects is an expansion of the auroral oval (Akasofu, 1966) to lower latitudes, together with an equatorward shift of MIT structure. The location of the equatorward edge of the auroral oval depends on the energy of the precipitating particles and the magnetospheric electric and magnetic fields (Kauristie et al., 1999). The zone of the intense high-latitude ionospheric irregularities expands from auroral/subauroral latitudes toward middle latitudes, occasionally down to 50°–55° magnetic latitudes (MLAT; Basu et al., 2001; Cherniak et al., 2015; Jakowski et al., 2008). Less expected and predictable thread for midlatitudes can appear from the opposite direction—it is a poleward expansion of the equatorial irregularities during geomagnetic storms.

Depending on the phase of a storm, local time (LT) in a particular longitudinal sector, season/solar flux conditions, and type of the storm-induced electric fields causing upward/downward equatorial plasma drifts, this combination of factors can support or suppress the equatorial plasma bubbles (EPBs) formation at various stages of a storm. First, there is a prompt penetration electric field (PPEFs) phenomenon, when high latitude electric fields directly penetrate to lower latitudes. The under-shielding PPEFs are eastward on the day and dusk side of the equatorial ionosphere (Fejer, 1991; Fejer et al., 1999; Kikuchi et al., 2008). During intense storms, the PPEFs of eastward polarity can cause large uplift of the equatorial ionosphere in the day and evening sectors that results in equatorial plasma diffusion along magnetic field lines to much higher altitudes and higher (poleward) latitudes with a drastic enhancement of the equatorial ionization anomaly (EIA), creating a daytime "superfountain" effect (Mannucci et al., 2005; Tsurutani et al., 2004, 2008). In the dusk sector, PPEFs can superimpose on the normal prereversal enhancement, resulting in larger upward $\mathbf{E} \times \mathbf{B}$ drifts (Fejer et al., 2008) and creating favorable conditions for Rayleigh–Taylor instability (Sultan, 1996). Generally, PPEFs are rather short-lived (∼30 min), but under specific conditions, the PPEFs can last for several hours (Huang et al., 2005). The second process is the disturbance dynamo electric fields (DDEFs) associated with large changes in the global thermospheric circulation originating from auroral heating (Blanc & Richmond, 1980). The DDEFs can reach the equatorial ionosphere as earlier as several hours after storm onset (Fuller-Rowell et al., 2002); they are long-lived and often become dominant during the recovery phase. The DDEFs are directed westward on the day and dusk sides and eastward on the night and dawn sides with largest magnitudes in the late-night sector (Scherliess & Fejer, 1997)—thus, they can support suppression of the normal post-sunset EPBs in the dusk sector and promote formation of fresh post-midnight/predawn EPBs during nighttime (Bhattacharyya et al., 2002; Hysell & Burcham, 2002; Yeh et al., 2001; Zakharenkova et al., 2015).

Thus, storm-time electric fields serve as a major source of the equatorial ionosphere modification, forcing significant changes in equatorial plasma drifts and typical EPBs generation. Previous studies reported occurrence of the intense EPBs associated with PPEF effects during different geomagnetic storms (Abdu, 2012; Carter et al., 2016; Kil et al., 2016; Li et al., 2018; Sori et al., 2021; Tulasi Ram et al., 2008; Zakharenkova et al., 2019). However, it is still impossible to predict how strong will the ionosphere's response be to a particular geomagnetic storm and when/where the storm-induced EPBs may occur around the globe. We know that occurrence of eastward PPEFs near local dusk can promote development of very intense EPBs whose longitudinal and latitudinal scales are much greater than those of normal EPBs. Sometimes, it can result in a huge plasma bite-out near the magnetic equator and formation of "super" plasma bubbles of unexpectedly large intensity whose latitudinal extent toward low/mid latitudes can occasionally reach 25°–35°MLAT (Basu et al., 2005, 2007; Cherniak & Zakharenkova, 2016; Foster & Rich, 1998; Greenspan et al., 1991; Huang et al., 2007; Ma & Maruyama, 2006; Martinis et al., 2015). Thus, Ma and Maruyama (2006) reported one of the first observations of the postsunset super plasma bubbles at midlatitudes (30°–34°N,

31°MLAT, Japanese sector) during the February 2000 geomagnetic storm. Huang et al. (2007) reported an occurrence of the deep plasma density depletions potentially associated with EPB at midlatitudes (up to 46° MLAT) of the American sector during the October 2003 superstorm. Cherniak and Zakharenkova (2016) reported the atypical plasma bubbles occurrence within the European sector during the June 2015 geomagnetic storm. Plasma density depletions were detected as poleward as 40°–45°N (35°–40°N MLAT) over 8 hr; they were associated to the plasma bite-out in the dusk sector over the West African longitudes. All these extreme plasma bubbles events were reported for intense space weather events during high solar activity period. Can geomagnetic storms during low solar activity trigger extreme EPBs too? Recent studies demonstrated that at low solar activity, even geomagnetic storms of moderate intensity can support formation of the storm-induced EPBs with such a large latitudinal extension (Aa et al., 2019; Zakharenkova & Cherniak, 2020). Furthermore, the storm-induced EPBs can easily occur even during the low bubble seasons. We should highlight that an occurrence of such super-bubbles is not an extremely rare or singular event—it can strike even several longitudinal sectors during the same storm. For example, for the June 2015 geomagnetic storm, the plasma bubbles at midlatitudes were registered first in the African/European longitudinal sector and then, several hours later, in the American sector, covering a wide-ranging longitudinal span (Cherniak & Zakharenkova, 2016; Cherniak et al., 2019). For another case of the September 2017 geomagnetic storm, the storm-induced EPBs expanded to midlatitudes were registered first in the American sector and near 12 hr later in the Asian sector (Aa et al., 2018, 2019). This phenomenon represents one of the most challenging space weather threads for Global Navigation Satellite System (GNSS)-based operation at midlatitudes due to lack of understanding and ability to predict (Doherty et al., 2004; Mrak et al., 2020; Zakharenkova & Cherniak, 2021).

The present research has the objectives to examine: (a) how far the storm-induced EPBs can extend during quite rare geomagnetic storms in low solar activity period; (b) if storm-induced EPBs occurring in different longitudinal sectors demonstrate the same or different scenarios/patterns of generation and evolution? To address these questions, we investigated an occurrence, evolution, and severity of the storm-induced ionospheric plasma irregularities at equatorial and middle latitudes of the American/Pacific sectors during the large geomagnetic storm that occurred on 25–26 August 2018, during low solar activity period.

2. Database

To examine an occurrence of the strong ionospheric irregularities initiated by the August 2018 geomagnetic storm, we analyzed measurements from 4,500+ ground-based GNSS stations with a specific Global Positioning System (GPS)-based index, ROTI (Rate of total electron content [TEC] Index change), proposed by Pi et al. (1997). ROTI expresses sharpness of the GPS/GNSS phase fluctuations caused by ionospheric irregularities and by strong spatial gradients of TEC. The ROTI values were calculated for every passage of GPS and GLONASS satellites (elevation above 20°) over a ground-based GNSS station. The ROTI values were referred to the intersection (ionospheric pierce point—ionospheric pierce point [IPP]) of the line-of-sight with the thin ionospheric layer at 350 km altitude. Further, the derived ROTI values with IPP coordinates were averaged into 0.5° latitude/longitude grid to create the high-resolution ROTI maps with a 15-min rate (for more details on the mapping technique, see Cherniak et al., 2018, 2019).

To assess the magnitude and spatial extent of the storm-induced ionospheric irregularities especially over oceans, we used observations from several Low-Earth-Orbiting satellites. First, we analyzed observations provided by the European Space Agency (ESA) Swarm mission of three satellites—Swarm A, Swarm B, and Swarm C—operating at polar orbits of ∼88° inclination. The Swarm B satellite had a higher orbit of ∼510 km altitude, whereas two other satellites were flying in a tandem (separation of ∼1° in space and ∼9 s in time) at ∼450 km orbit altitude. We used in situ electron density (Ne) data from Langmuir probe instrument and field-aligned currents (FACs) estimated from the Swarm magnetometer data (Lühr et al., 2015; Stolle et al., 2017). Second, we used in situ ion density (Ni) and drifts measured by the Ion Velocity Meter instrument onboard the Defense Meteorological Satellite Program (DMSP) F16 satellite at a much higher orbit altitude (∼860 km). As of 26 August 2018, the local times of the ascending and descending nodes for the F16 satellite were ∼15.8 LT and ∼3.8 LT, respectively. Third, we used observations from Jason-2 and Jason-3 missions flying at a circular orbit at ∼1,330 km altitude with an orbit inclination of ∼66°. Measurements provided by a dual-frequency nadir-looking radar altimeter operating at 13.575 GHz (Ku-band) can be used to estimate an ionospheric electron content (EC) below the Jason orbit (∼1,330 km) but only over the ocean surface. Measurements provided by a dual-frequency onboard GPS receiver can be used to estimate topside electron content above the Jason orbit. More details on processing

nadir-looking KU and up-looking GPS measurements can be found in (Cherniak & Zakharenkova, 2019). Additionally, we utilize ionosonde measurements with a 15-min cadence from two ground-based digisondes located at North America midlatitudes—Pt. Arguello (34.8°N; 120.5°W; 42.3° MLAT), and at low latitudes of the North Pacific—Lualualei (21.4°N; 158.2°W; 20.0° MLAT).

3. The 25–26 August 2017 Geomagnetic Storm: Space Weather Conditions

The strong (G3) geomagnetic storm on 25–26 August 2018 occurred close to the end of the twenty fourth solar cycle at the background of the low solar flux ($F_{10.7} \sim 70$) and, correspondingly, at the low level on the ionospheric plasma density. This storm is considered as the third largest geomagnetic storm of the twenty fourth solar cycle in terms of the Dst minimum excursion (Dst minimum reached −175 nT). It is expected that ionospheric response to a space weather event can be quite significant under such conditions.

This storm was produced by a slow CME on 20 August 2018, which arrived the Earth magnetosphere on 25 August 2018. Figure 1 presents high-resolution (1-min) variations of solar wind, interplanetary magnetic field (IMF) vertical component, and geomagnetic activity indices such as AE, SYM-H, and Kp (3 hr) during 24–27 August 2018. The symmetric H component (SYM-H) index can be treated as a high-resolution (1-min) Dst index and represents ring current intensity (Iyemori, 1990; Iyemori & Rao, 1996). The auroral electrojet (AE) index represents global electrojet activity in the auroral zone. The IMF southward turning occurred after 14 UT on 25 August 2018 (Figure 1a). The IMF vertical component Bz remained steady negative during more than 17 hr from 15:30 UT on 25 August till 09:00 UT on 26 August, and the peak Bz component reached −16 nT near 05 UT on 26 August 2018. During this period, the main phase of the storm developed starting from ∼18 UT on 25 August and the SYM-H index dropped to a minimum of −205 nT at ∼07:10 UT on 26 August 2018 (Figure 1f). The

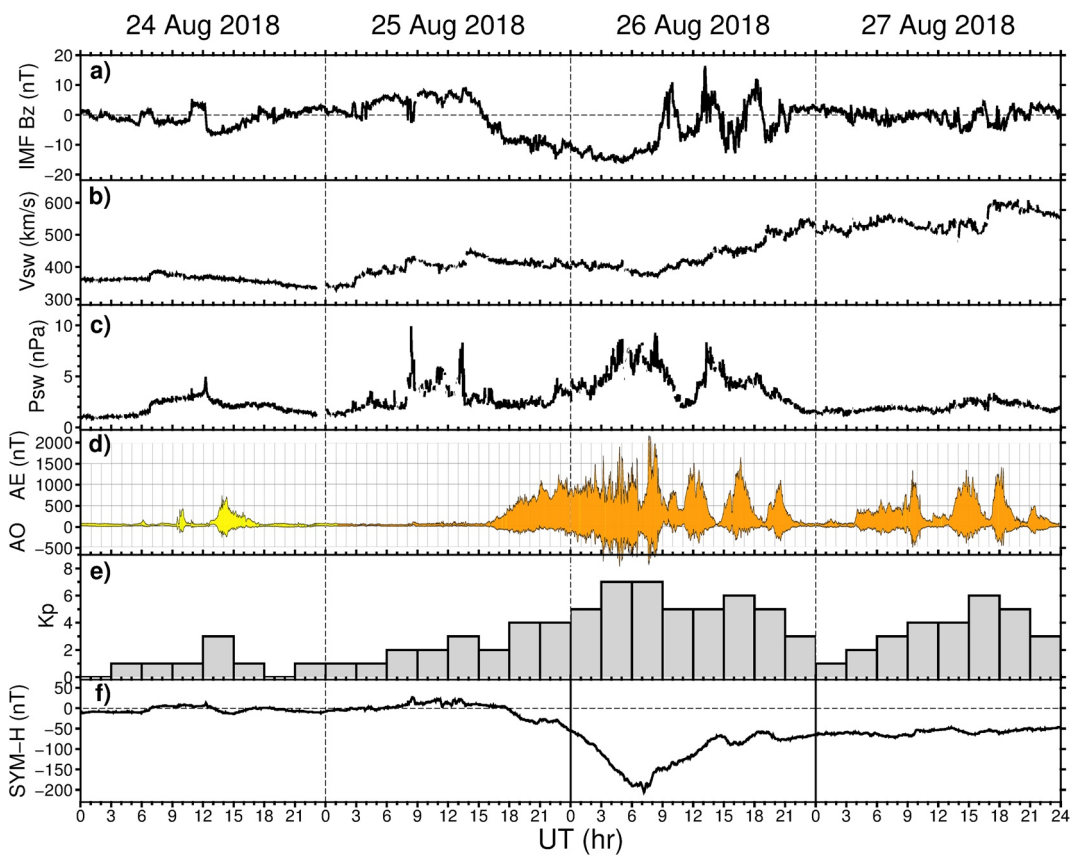

Figure 1. Geomagnetic conditions during 24–27 August 2018: (a) interplanetary magnetic field Bz component, (b) velocity and (c) dynamic pressure of the solar wind, (d) auroral electrojet indices AE and AO, (e) Kp index, and (f) symmetric H component index.

provisional hourly Dst index had a minimum value of −175 nT at that time. The AE index increased above 500 nT after 18 UT on 25 August and the AE peaks exceeded 1,500–2,000 nT during 02–09 UT on 26 August 2018, concurrently with the solar wind pressure increase. The solar wind speed increased from ∼340 km/s at 00–03 UT to ∼450 km/s at 14 UT on 25 August, then fluctuated between ∼410 and ∼380 km/s during the main phase of the storm and further gradually increased to ∼540 km/s at 22 UT on 26 August. During the main phase of storm, the geomagnetic three-hourly Kp index reached 7+ (Figure 1e), and the storm was classified as a strong, G3-level storm in the NOAA Space Weather scale.

4. Results and Discussion

First, we analyzed an occurrence and development of the storm-induced ionospheric irregularities that were identified through their impact on the received GNSS signals (here, phase scintillations) using the ground-based GNSS ROTI observations. Figure 2 presents an overview of the ionospheric irregularities development in the American longitudinal sector with the progression of the main phase of the storm. At 01:30 UT on 26 August 2018, analysis of the ROTI map (Figure 2) indicates the following: (a) an absence or very low intensity of ionospheric irregularities (small ROTI magnitudes marked by dark-blue color) at midlatitudes; (b) intense ionospheric irregularities with high ROTI magnitudes (ROTI > 0.8–1.0 TECU/min, yellow–red color) at high latitudes of both hemispheres, and (c) an occurrence of the medium-intense irregularities at low latitudes, over the Western coast of South America, after the sunset terminator passage. The AE index increased rapidly above 500 nT after ∼18 UT on 25 August, and during the main phase of the storm it had steadily high values of ∼1,000 nT with peaks up to 1,500–2,000 nT. With such a high level of auroral activity till ∼08 UT, the auroral zones with intense ionospheric irregularities expanded further equatorward to ∼50°N and ∼65°S, that is, ∼55° MLAT in both hemispheres. In the post-sunset equatorial ionosphere of the American sector, the ionospheric irregularities developed over the Western Coast region (60°–90°W) during 01–04 UT with a latitudinal extent of ±15°MLAT from the magnetic equator. We should note that August is a climatological low season for typical postsunset EPBs in the South America region, especially during solar minimum conditions (Retterer & Gentile, 2009 [Figure 2a]; Xiong et al., 2010 [Figure 6]). It is interesting that under the long-lasting, steady southward IMF Bz, the storm-induced post-sunset EPBs occurred only over the Western South America region and they were not developed over Eastern South America (30°–60°W), whereas the post-sunset EPBs were also detected over the Western African region (15°W–5°E) during 22–02 UT (not shown here). Suddenly after ∼04 UT, the northernmost part of the equatorial ionospheric irregularities started stretching northward along the Western Coast of North America toward high latitudes and the auroral irregularities zone. At ∼05 UT, the narrow zone of the stretched ionospheric irregularities reached ∼40°N (45° MLAT). We have a very sparse coverage of the equatorial region over 80°–120°W longitudinal span due to absence of the ground-based GNSS stations here. Thus, the ground-based GNSS observations could not clarify what happened in the conjugate sector and equatorial zone of that region during that particular time. After ∼05 UT, the sunset terminator reached the Hawaii longitude zone (∼150°W). The GNSS ROTI observations from the ground-based stations located at several islands in the Pacific Ocean revealed an occurrence of the storm-induced post-sunset irregularities over 160°–140°W longitudinal span (Figure 2). The intense ionospheric irregularities were observed at both sides from the magnetic equator and their latitudinal extent was up to 25°–27° MLAT. Here, the signatures of the ionospheric irregularities persisted for many hours till the morning. Thus, the analysis of the ROTI maps revealed two zones with the storm-induced EPBs generation within the American/Pacific sector.

Figure 3 provides a satellite view on the storm-induced ionospheric irregularities development as detected by in situ plasma density measurements onboard the Swarm and DMSP satellites that crossed the American/Pacific sector on 26 August 2018. The Swarm B satellite flying at ∼510 km altitude was the first one to encounter the considered sector. The equatorial crossing local time was ∼21.6 LT, that is, the very favorable time to detect the fresh post-sunset EPBs, if they occur. During the overpasses #1–2 (Figure 3c), the satellite did not detect any presence of the ionospheric irregularities reaching this topside altitude in the equatorial region over 40°–65°W longitudinal span. This agreed well with the ground-based ROTI observations revealing that the storm-induced postsunset plasma bubbles were not developed in the eastern or central regions of South America during the main phase of the storm (Figure 2). The next pass #3 at 3.0–3.8 UT was near 88°W crossing near the western coast of South America. Here, for the first time, the satellite detected a plasma depletion close to the magnetic equator and two even deeper depletions located near 20°S (∼10° MLAT) and 38°S (∼28° MLAT) in the Southern

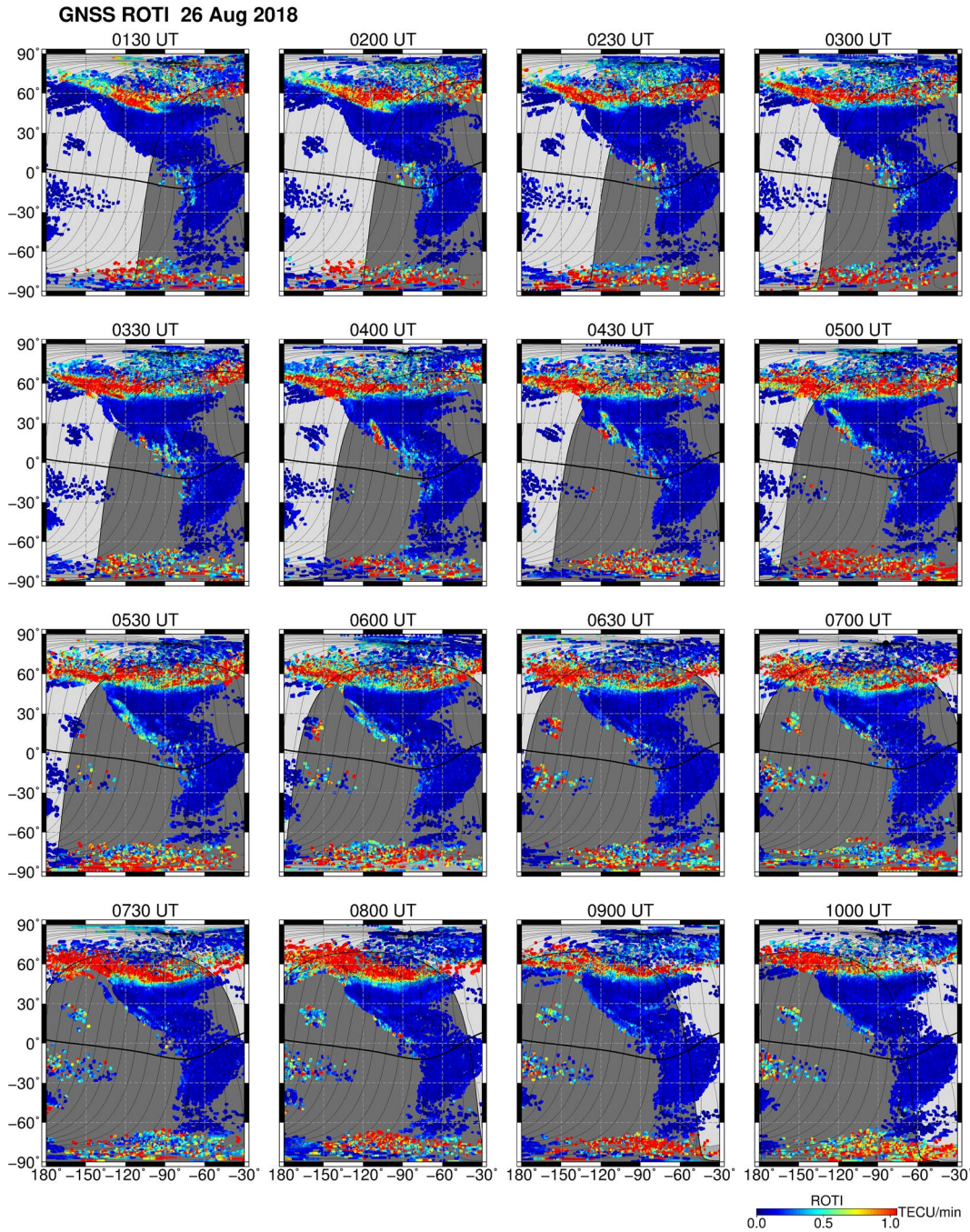

Figure 2. Global Navigation Satellite System Rate of total electron content (TEC) Index change (ROTI) maps for specific times on 26 August 2018. The thick black line marks the magnetic equator, thin lines–magnetic field lines. The shaded area shows nighttime. High ROTI values (intense red color) depict severe ionospheric irregularities occurrence at equatorial and auroral zones.

Hemisphere. The next pass (Figure 3c, pass #4) was near 112°W crossing mainly the Pacific Ocean and near the western coast of North America. The satellite encountered the multiple plasma depletion structures at equatorial and low latitudes, as well as a well-isolated depletion near 20°N (~28° MLAT) in the Northern Hemisphere, close to the Gulf of California. The next overpasses #5–7 detected plasma bite-outs near the magnetic equator and multiple deep plasma density depletions developed over a broad range of latitudes (±20°MLAT) at both sides from the magnetic equator. The Swarm B overpasses #8–9 demonstrated an absence of the ionospheric irregularities in the equatorial region over 129°–153°E, in the Western Pacific Ocean.

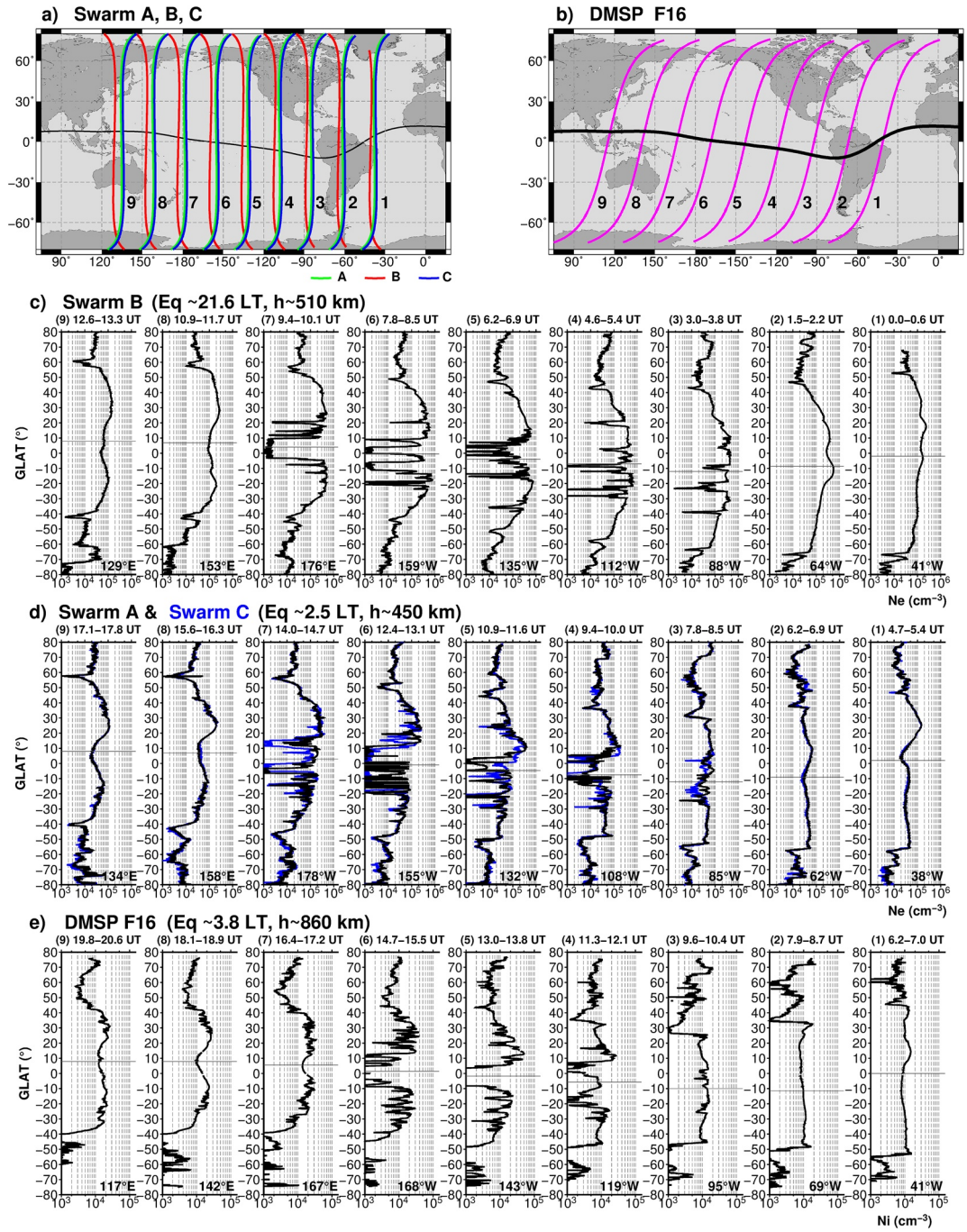

Figure 3. Ionospheric irregularities as detected by in situ plasma density observations onboard Swarm and Defense Meteorological Satellite Program (DMSP) F16 satellites during 26 August 2018. Global map with (a) Swarm A, B, and C satellites passes and (b) DMSP F16 passes. Variation of in situ electron density Ne as a function of geographical latitude along (c) Swarm B passes at ~510 km altitude, (d) Swarm A & Swarm C tandem passes at ~450 km altitude, and (e) variation of in situ ion density Ni as a function of geographical longitude along DMSP F16 passes at ~860 km altitude. Horizontal gray line marks the magnetic equator latitude. Graph captions show (top) the satellite pass number, UT interval, and (bottom) geographic longitude of equatorial crossing for each pass.

The tandem of Swarm A and C satellites nearly repeated the Swarm B overpasses in the same region, but ~5 hr later in time. The satellites operated at a lower altitude (~450 km) than the Swarm B. The equatorial crossing local time for these satellites was ~2.5 LT, thus, the satellites could detect the EPBs either persisted from the postsunset period or freshly generated in the post-midnight. The first passes #1–2 (Figure 3d) confirmed again the

absence of the ionospheric irregularities over the eastern/central regions of South America. The next passes #3–7 demonstrated the occurrence of the intense ionospheric irregularities along the very same passes as Swarm B did it earlier—the large-scale plasma structuring was observed during that night over the most part of the Pacific Ocean from 85°W to 180°W. The ionospheric irregularities noticeably extended from the equatorial zone toward low and middle latitudes in both hemispheres.

A couple of hours after the Swarm mission passage, the DMSP F16 spacecraft encountered the same region. It had a polar orbit with an altitude of ∼860 km, roughly 400 km higher than the Swarm tandem, and its orbit had a lower inclination than those of Swarm. The equatorial crossing time was ∼3.8 LT, thus, satellite could potentially detect the EPBs that reached that high altitude and survived through the nighttime. First two passes of DMSP F16 over the American sector (Figure 3e, passes #1–2) detected progressive deepening of the MIT at ∼40°–45° MLAT and sharp plasma density structuring poleward from the MIT location, but no signatures of the topside ionospheric irregularities were found in the equatorial sector. Interestingly, that pass #2 intersected the equatorial region of Western South America (∼69°W), where signatures of the equatorial irregularities were detected by ground-based GNSS ROTI observations earlier at time in the postsunset (∼01–06 UT), but when DMSP F16 overpassed this region at ∼8.5 UT, both ROTI and DMSP satellite observations did not reveal such signatures. That means that either the apex altitude of the EPBs developed in this region did not reach the DMSP orbit altitude, or EPBs have been already decayed at that time. The next pass #3 crossed the magnetic equator near 95°W and detected signatures of the plasma depletions that located symmetrically at the both sides from the magnetic equator with a latitudinal extension up to ∼10°–15° MLAT, which corresponded to the EPB apex altitude of ∼1,400 km. During the overpass #4 near 119° W longitude, DMSP F16 encountered the strongly disturbed equatorial ionosphere with multiple large-scale structures that already reached this high altitude—two large-scale deep plasma depletions located symmetrically at the both sides from the magnetic equator within ±5–15° MLAT provided evidence of the strong fountain effect that uplifted the equatorial ionosphere during the storm. Several plasma density depletions were observed even more poleward from the major EPB structures reaching as high as ∼20–25°MLAT in both hemispheres. One of the most poleward depletions observed in the Northern Hemisphere was located close to the Gulf of California, similar to the large depletion that was detected by the Swarm B spacecraft ∼7 hr ago (Figure 3c, pass #4). That means that this distant plasma depletion structure was persisted for many hours and reached ∼860 km altitude. The next pass #5 was near 143°W and it clearly detected a large plasma bite-out near the magnetic equator and multiple plasma density depletions transported far away from the equator by the enhanced fountain effect action. These structures moved as poleward as ∼30° MLAT in both hemispheres, rather close to the MIT position that shifted in the opposite, equatorward direction with the storm development. The DMSP overpass #6 was over the central Pacific Ocean near 168°W and it also detected a plasma bite-out near the magnetic equator and the strongest plasma density structuring extended over the large range of latitudes from the equator toward midlatitudes for both hemispheres. In the Northern Hemisphere, plasma density disturbances were observed up to ∼40°N with multiple plasma density depletions within an area of 20–30°N, that is, in the vicinity of Hawaii islands. The ROTI maps revealed an occurrence of the storm-induced ionospheric irregularities here starting from ∼06 UT till at least 10 UT on 26 August 2018 (Figure 2); later in time, Swarm B detected plasma density depletion in this region at ∼08 UT (Figure 3c, pass #6) and the tandem of Swarm A/C satellites near 13 UT (Figure 3d, pass #6). DMSP F16 detected clear signatures of intense ionospheric irregularities in this region at ∼15 UT—thus, these storm-induced irregularities persisted here for a prolonged period from postsunset at least till ∼04 LT in the morning. During the next passes #7–8, DMSP F16 still registered ionospheric plasma density perturbations but of much smaller intensity at low/middle latitudes of both hemispheres, as well as signatures of the previous action of the enhanced fountain effect forming the EIA crests and trough near the equator, these mainly daytime signatures of the EIA still persisted at such high altitudes of the night-time equatorial ionosphere (∼04 LT).

Thus, Figure 3 illustrates complex signatures of the topside ionospheric irregularities development as detected independently by two different missions with in situ plasma density measurements (Swarm and DMSP) well separated in time and altitude. We should emphasize that in situ plasma probe measurements represent 1-D horizontal slices of ionospheric plasma and can detect ionospheric structures at satellite orbit altitude only.

Figure 4 compares two events of the ionospheric irregularities extension from equatorial toward higher latitudes as detected rather close in space and in time in the Northen Hemisphere: (a) in the North America region near

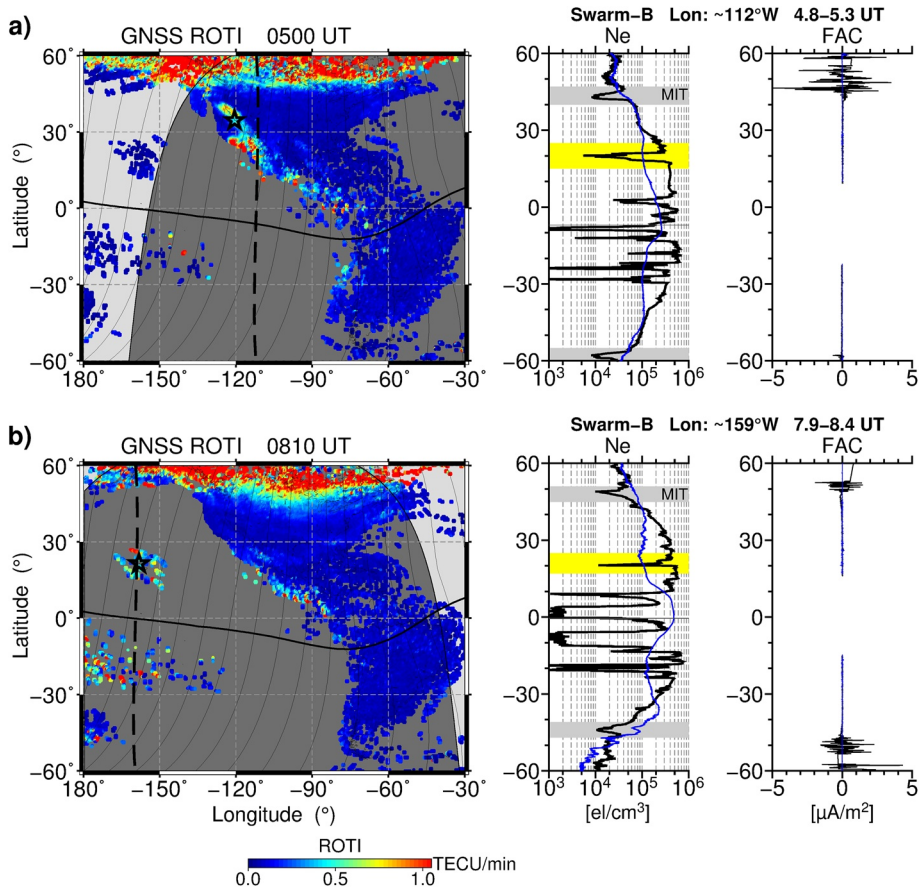

Figure 4. Two cases of the equatorial ionospheric irregularities expansion toward higher latitudes detected in (a) North America and (b) Hawaii: ground-based Rate of total electron content (TEC) Index change maps showing an occurrence of the ionospheric irregularities with the superimposed overpass of Swarm B satellite (black dashed lines), variation of in situ electron density Ne and field aligned currents as a function of geographical latitude along the satellite pass; black line shows measurement during the storm on 26 August, blue line–the reference for the prestorm observations on 25 August 2018. Gray shading shows main ionospheric trough position in Swarm Ne observations. Black asterisks on the maps show digisondes location closest to Swarm overpasses in North America and Hawaii.

California and (b) in the Pacific Ocean near Hawaii. In the first case (Figure 4a), the ground-based ROTI map revealed a narrow, elongated area of the intense ionospheric irregularities that stretched along the western coast of North America close to California and the Gulf of California toward the auroral irregularities zone. Thanks to the favorable orbit configuration for that day, the Swarm B intersected part of this structure and detected a large-scale plasma density depletion at ~20°N (~27° MLAT) near the Gulf of California (yellow shading in Figure 4a). This depletion was rather isolated from the multiple depletions observed in the equatorial region of the Pacific Ocean, but at the same time, it was well isolated from the MIT location (gray shading in Figure 4a). To support the MIT localization, we also provided Swarm FAC observations along the tracks. The downward Region-2 FACs close through the low ionospheric conductivity MIT region, thus, the FAC observations from Swarm satellite magnetic field measurements could be complementary used to determine the MIT position. The provided results represent small-scale FACs variations (no filter or smoothing applied to synthesize larger scale FACs) for a single-satellite estimate. We can see that intensification in FAC observations coincided well with the MIT position determined by the concurrent in situ Ne measurements. Comparison with the quiet-time conditions on the previous day (blue lines) demonstrates a rather smooth Ne variation along the track without any plasma density depletions at equatorial and low latitude regions, as well as a single-peak enhancement near the magnetic equator that corresponds to the typical quiet-time behavior of the EIA in the night-time. The background Ne level at low and middle latitudes during the storm day was much higher than that of the quiet-time conditions under the action of the enhanced fountain effect. For the second event (Figure 4b), we observe a similar signature of plasma density depletion

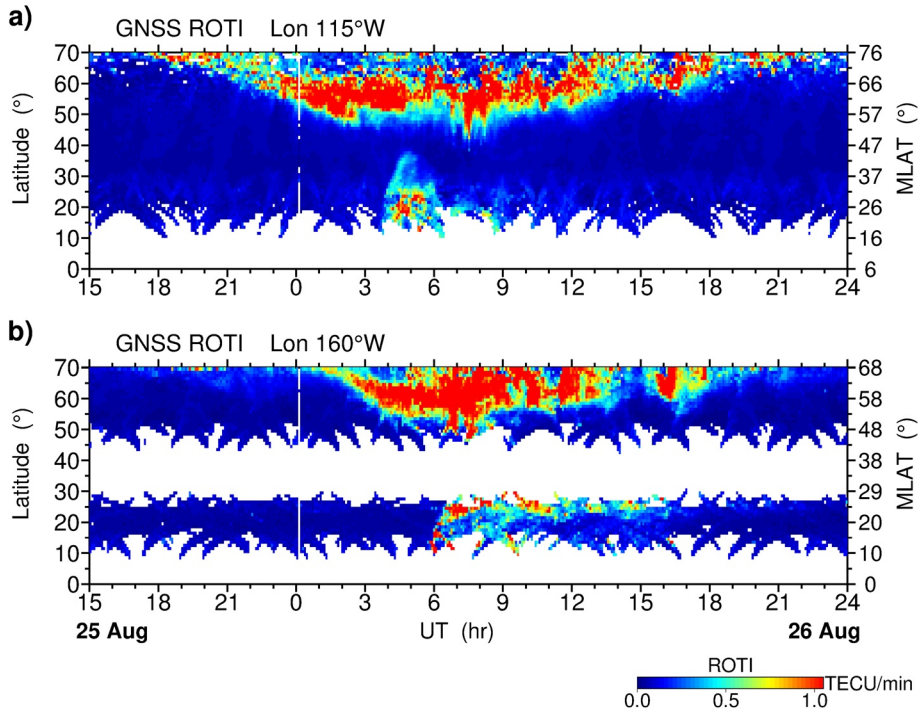

Figure 5. North–south cross-sections (keograms) representing the spatio-temporal features of the storm-induced ionospheric irregularities as detected in Global Navigation Satellite System Rate of total electron content (TEC) Index change along (a) 115°W and (b) 160°W longitudes for a time interval of 15–24 UT on 25–26 August 2018. Vertical axes show (left) geographic and (right) geomagnetic latitudes. White color depicts empty cells due to lack of actual observations.

(yellow shading) over Hawaii, but it had a slightly smaller magnitude in Swarm Ne density than that of the first event over North America, and it was observed near 20°N (~20° MLAT), more close to the magnetic equator.

To illustrate temporal evolution of the storm-induced sirregularities for these two events, we plot the north–south cross-sections (keograms) of the GNSS ROTI maps constructed along 115°W and 160°W longitudes during 25–26 August 2018 (Figure 5). These keograms, plotted as a function of geographic latitude and UT time, show the averaged values across a narrow longitudinal range (±3.5°) around the considered longitude. Figure 5a demonstrates that in the North America sector, the ionospheric irregularities developed at high latitudes after ~18 UT on 25 August that coincided to the AE index increase up to ~500 nT. In the next hours, with the progression of the main phase of the storm and further AE rise to ~1,000 nT, the zone with intense auroral irregularities expanded equatorward and reached ~50°N (57° MLAT) at 02–03 UT on 26 August 2018. During ~04–06 UT, the signatures of the ionospheric irregularities of moderate-to-intense magnitude were registered at low/mid latitudes of the considered sector. These irregularities, well separated from the auroral ones, were observed over ~15°–35°N, thus reaching ~35°–42° MLAT in the North America sector. Further into the Pacific Ocean sector near the longitude of Hawaii (Figure 5b), the intense auroral irregularities expanded even greatly in the equatorward direction, reached ~50°N (~48°–50° MLAT) during the main phase of the storm. After ~06 UT on 26 August, the intense ionospheric irregularities started to develop at much lower latitudes ~10°–28°N (~10°–28°MLAT). We cannot determine the upper boundary of this extent due to a large data gap at 28°–48°N. These irregularities were characterized by a much longer duration in time—from ~06 till ~16 UT that covered the whole postsunset–nighttime period of local time. Thus, we observed two types of ionospheric irregularities extensions toward low/middle latitudes: (a) in the North American sector, these irregularities occurred in a burst-like mode during postsunset period (20–23 LT), rapidly reaching higher latitudes (up to 42° MLAT), but they were observed rather short time, roughly 2 hr from 04 UT till 06 UT; (b) in the Pacific Ocean sector near Hawaii, the ionospheric irregularities occurred after local sunset (~19 LT) and persisted many hours for the entire night till sunrise; their latitudinal extent reached at least ~28° MLAT.

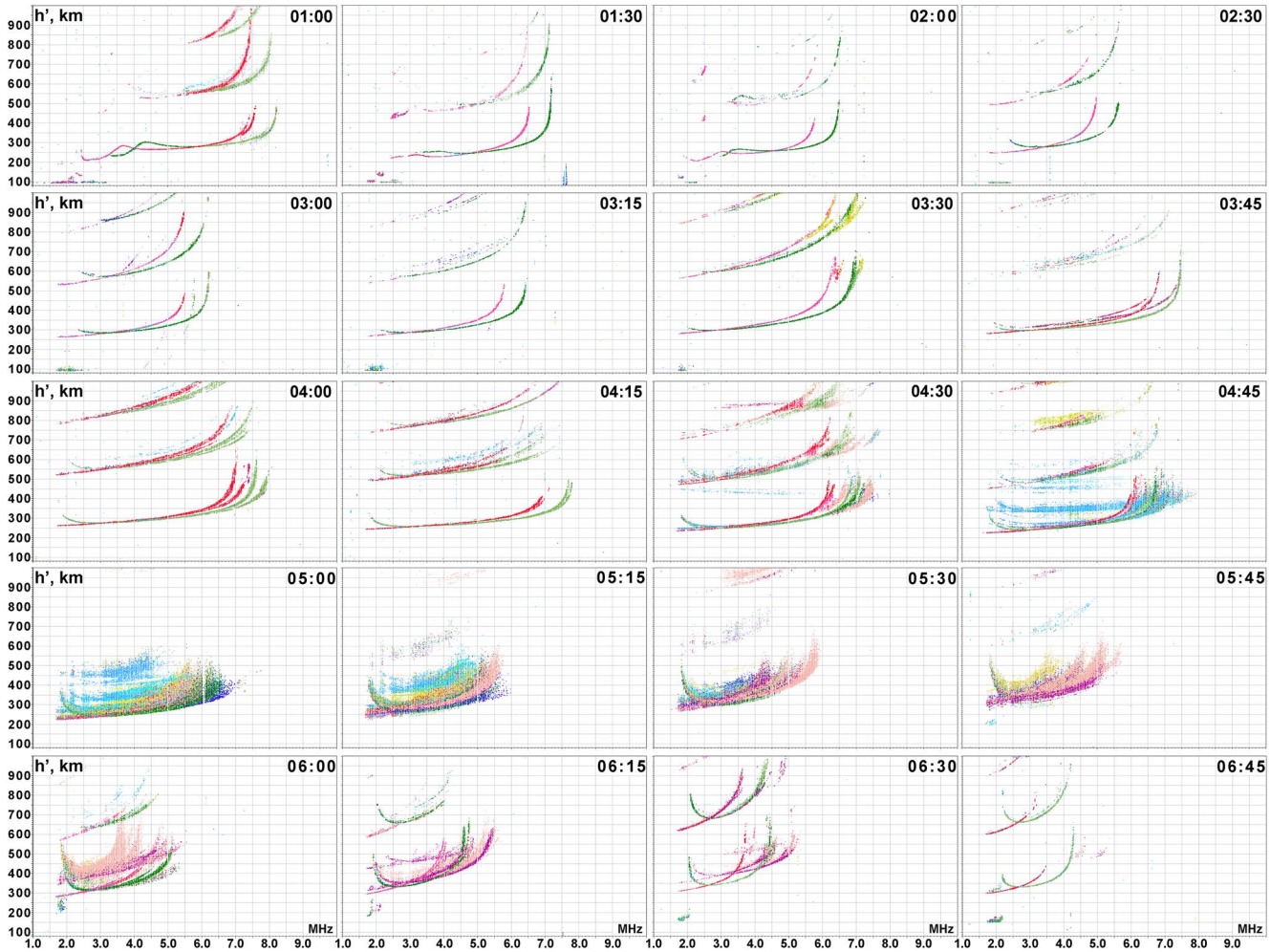

Figure 6. Vertical ionograms recorded by the Pt. Arguello digisonde (34.8°N; 120.5°W; 42.3° magnetic latitude) in California, USA, during 01–07 UT on 26 August 2018. The O-mode polarization is shown by red trace, the X-mode–by green trace, and diffuse echoes correspond to spread-F conditions.

Further, we examined signatures of the revealed storm-induced ionospheric irregularities in the records of the ground-based stations vertically sounding the ionosphere. For the first case, the nearest station was the Pt. Arguello digisonde (34.8°N; 120.5°W; 42.3° MLAT) located in California, for the second one—the Lualualei digisonde (21.4°N; 158.2°W; 20.0° MLAT) located in Hawaii. Geographical location of both digisondes was shown by black asterisks in Figure 4. The digisondes provide digital ionogram records, which show variations of the virtual height of reflection from the ionospheric layers as a function of the radio frequency, h′(f). Both digisonde stations obtained one ionogram recording every 15 min Figure 6 presents series of the ionograms recorded by the Pt. Arguello digisonde during 01–07 UT on 26 August 2018. First two rows of ionograms represent rather clear, standard ionograms with well-identified ordinary (O–mode polarization) and extraordinary (X–mode) traces. At 0300–0315 UT (~19.5 LT), the F2 layer critical frequency (foF2) values were 5.0 and 5.5 MHz, respectively, to that moment, it was gradually reduced from 7.5 MHz recorded at 0100 UT (17 LT). After 0330 UT, the foF2 values started to increase again, a signature of the evening-time enhancement of the F2 layer ionization at midlatitudes during the storm. At 0400 UT, the ionogram recorded an appearance of the additional traces close to the principle traces and foF2 increased to 7 MHz. At 0430 UT, the ionogram shows an occurrence of the Frequency Spread–F near the critical frequency seen in both O–mode and X–mode traces. During 05–06 UT (~21–22 LT), the ionograms show diffuse reflections of the Mixed Spread–F type combining Frequency and Range Spread-F signatures with broad reflections in both frequency and range. Such Spread-F conditions represent a very atypical phenomenon for the midlatitude ionosphere; potentially, it can occur during geomagnetic disturbances when the auroral irregularities zone expanded greatly toward midlatitudes. At the considered location (~35°N, ~42° MLAT),

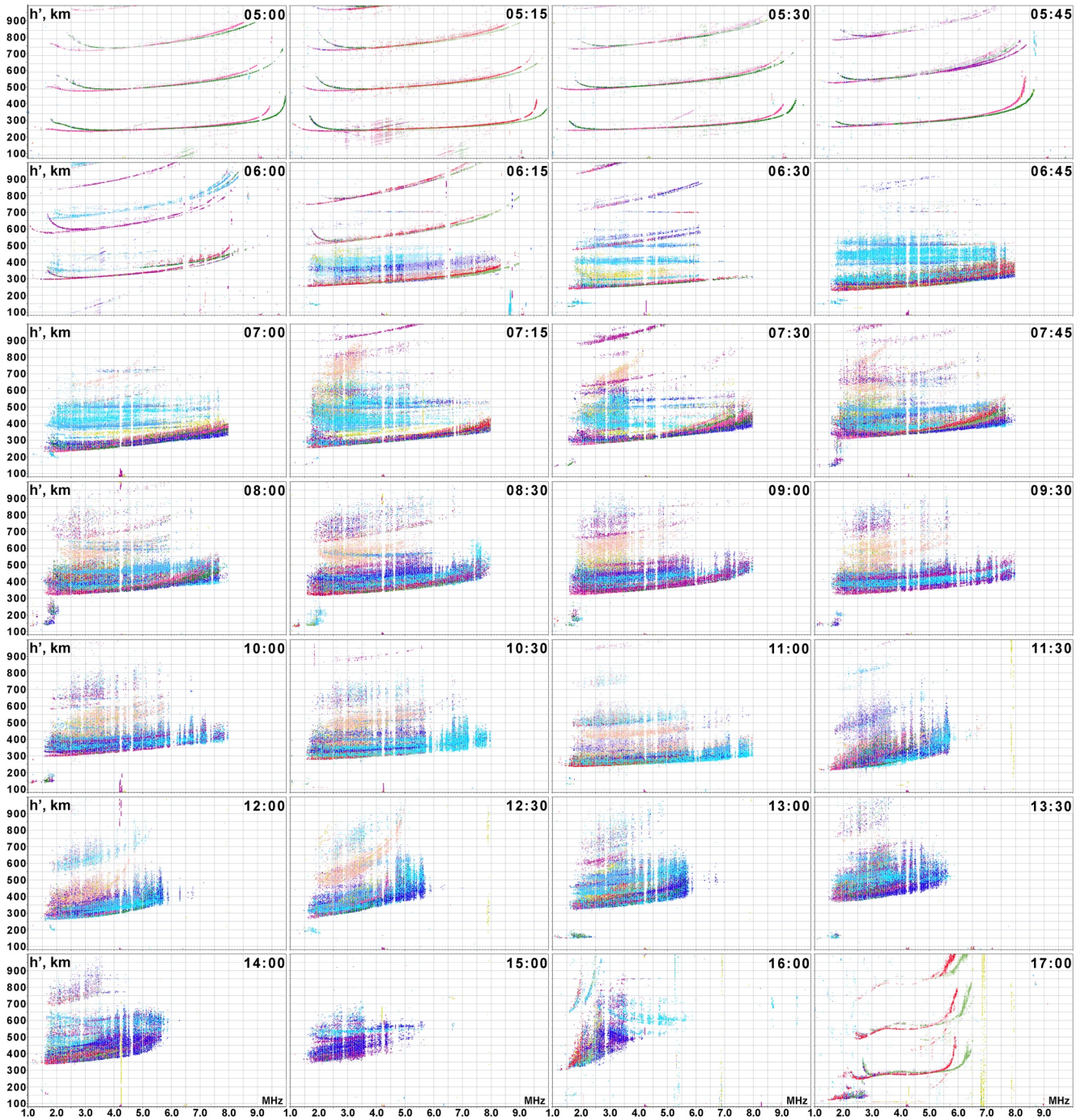

Figure 7. Vertical ionograms recorded by the Lualualei digisonde (21.4°N; 158.2°W; 20.0° magnetic latitude) in Hawaii, USA, during 05–17 UT on 26 August 2018. The O-mode polarization is shown by red trace, the X-mode–by green trace, and diffuse echoes correspond to spread-F conditions.

the Spread-F was registered during roughly 1 hr, and it coincided well in time and space with the streamed plasma density irregularities from low latitudes toward an auroral zone along the western coast of North America as observed in GNSS ROTI (Figures 2 and 5a).

Figure 7 presents series of the ionograms recorded by the Lualualei digisonde in Hawaii during 05–17 UT on 26 August 2018. Here, the first ionograms correspond to the pre-sunset period and they show clear, sharply defined traces with the foF2 values changing from 9.5 to 8.5 MHz. At 0615 UT (~20 LT), the ionogram shows the first occurrence

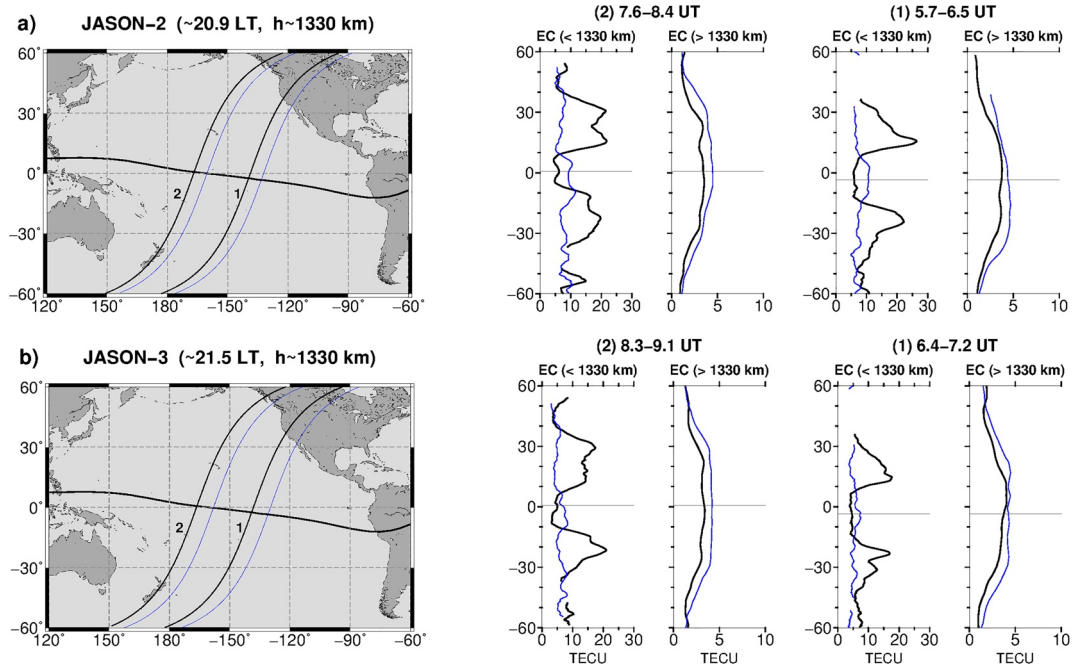

Figure 8. Variation of electron content below and above orbit for (a) Jason-2 and (b) Jason-3 satellites for two consecutive overpasses of the Pacific Ocean on 26 August 2018. Black line shows measurement during the storm day, blue line–the reference for the prestorm observations on 25 August 2018.

of the Range Spread–F. Further, the Range and Mixed Spread-F signatures were observed at all ionograms till 1645 UT (~06 LT). Thus, in contrast to the first event where the Spread–F was observed only short amount of time (~1 hr) and associated with the short-term passage of the streamed ionospheric irregularities overhead the digisonde; in Hawaii (~21°N; 20° MLAT), the Spread-F conditions were associated with the post-sunset equatorial ionospheric irregularities occurred at ~20 LT and persisted the entire night till ~06 LT. Aside from the fact that the August month corresponds to a season with a very low occurrence probability for postsunset EPB in both Pacific and American sectors, we should note that August 2018 was in the solar minimum conditions with $F_{10.7}$ near 70 sfu, thus, the EPBs can occur with even smaller occurrence probability due to deficiency of strong prereversal enhancement upward drifts (e.g., Fejer et al., 1999). The background density as well as the F layer height has also lower values in the solar minimum, so, typical EPBs capable to reach rather limited apex altitudes below 500–600 km (e.g., Joshi et al., 2021).

Figure 8 presents variations of electron content (EC) derived below and above the orbits of Jason-2 and Jason-3 satellites that overflied the Pacific Ocean nearly one after another during evening local time (~21 LT) on 26 August 2018. The satellites provide observations of "ionospheric" EC (100–1,300 km altitudinal range) from altimeter observations below the satellite orbit but only above the ocean surface and "plasmaspheric" EC (1,300–20,000 km altitudinal range) from topside onboard GPS observations. For the previous, quiet-time day, the down-looking EC was near 5–10 TECU, the up-looking EC associated with the plasmaspheric density population increase gradually from ~1 TECU at higher latitudes to ~4 TECU above the equator. During the geomagnetic storm, the pattern of the Jason-derived EC behavior dramatically changed. Most significant changes were registered for down-looking, ionospheric EC observations and we should highlight a strong enhancement of ionospheric EC at equatorial and subequatorial latitudes. The EC distribution modified into a broad minimum near the magnetic equator and two widely spread crests centered near 20° MLAT in both the Northern and Southern hemispheres. Within these enhancement zones, the ionospheric EC increased by ~3–4 times from ~5–7 TECU to ~20–25 TECU. These large enhancements of the evening EIA were observed by both satellites within a longitudinal range of 180°W–130°W of the Pacific Ocean. The pass #2 was in the closest proximity to Hawaii; the results indicated that this region was within the northern crest of the enhanced EIA. The accompanying feature was a large-scale decrease of ionospheric EC just above the magnetic equator within ±10° MLAT, where EC dropped from ~10 to ~4 TECU as compared to the quiet-time conditions. Location of the trough-like zone with the decreased EC agreed well with the plasma bite-out locations detected by Swarm and DMSP satellites cross-sections

(Figure 3). For the plasmaspheric EC, we found that storm-time values were below the quiet-time conditions that can be explained by the vertical redistribution of the plasma density within the ionosphere-plasmasphere system and plasmasphere contraction during the main phase of storm. Thus, the Jason observations confirmed that during the prolonged southward IMF Bz conditions, the storm-time eastward PPEFs uplifted drastically the equatorial ionosphere that led to the broad plasma density depletion near the magnetic equator and widely spread EIA peaks separated by ∼30°–40° in latitude—that are signatures of the "superfountain" effect (e.g., Tsurutani et al., 2004, 2008). The postsunset EPBs developed in the destabilized equatorial F region, and they were able to reach significantly larger apex altitudes. Thus, the ionospheric irregularities detected by ROTI maps and in situ satellite observations were found to occur between the widely spread crests of the enhanced EIA. The Hawaii region happened to be within the large EIA crest in the Northern Hemisphere, and storm-induced EPBs well developed here, thus, reaching atypically large latitudes (20°–25° MLAT) for solar minimum conditions.

5. Conclusions

We analyzed the ionospheric response to the 25–26 August 2018 geomagnetic storm, which occurred at the background of very low solar activity. The prominent feature of this response was development of the storm-induced ionospheric plasma density irregularities over broad latitudinal ranges from equatorial toward middle latitudes. Development of these irregularities was supported by superimposing of PPEF event of long duration, strong fountain effect that largely uplifted the equatorial ionosphere and led to the enhanced and widely spread EIA peaks, and positive ionospheric storm, which was observed distinctly in the Jason-derived ionospheric EC and ionosonde observations. We revealed two different patterns of the equatorial ionospheric irregularities expansion toward middle latitudes during the geomagnetic storm: (a) storm-induced EPBs developed over a large latitudinal extent, and (b) narrow channel of the ionospheric irregularities stretched in the northwestward direction from the EPB location toward the MIT.

In the first case, perturbed electric fields in the dusk sector can initiate dramatic development of post-sunset EPBs due to large uplift of the equatorial ionosphere to high altitudes and the EIA superfountain effect. Severe plasma bite-outs can significantly enlarge a latitudinal extent of the storm-induced EPBs to both sides from the magnetic equator; this latitudinal extent can exceed all climatological-based expectations. For the considered storm, such EPBs were observed over Hawaii region, thus, reaching atypically large latitudes (20°–25° MLAT) for solar minimum conditions.

The second type represents a rare case of further evolution of irregularities of the first type. Occasionally, part of the storm-induced, largely extended EPBs can be involved into northwestward plasma transportation likely under the action of enhanced westward drifts at midlatitudes. The northernmost part of the extended plasma depletion started to stretch further northward, tilted away from the magnetic field lines direction, and moved further in a poleward northwestward direction toward the MIT and auroral irregularities zone. Such channels of plasma depletions moving poleward from low latitudes were observed in the North American sector for several other geomagnetic storms, for example, ionospheric irregularities moved in quite the similar way along the western coast of North America for the storm that occurred in June 2015 (Cherniak et al., 2019), or more close to the center and eastern coast of North America for events in May 2017 and September 2017 (Aa et al., 2019; Mrak et al., 2020; Zakharenkova & Cherniak, 2020). It also remains unclear if the same scenario with a poleward transportation of EPBs from low-to mid-latitudes took place during other extreme events when plasma depletions were detected at very high MLAT with anomalously high apex estimates of ∼6,000–7,000 km (e.g., Huang et al., 2007; Martinis et al., 2015).

The ionospheric irregularities of the first type can persist numerous hours from sunset till sunrise over an area of their initial development with some westward drift. For the second type, the ionospheric irregularities can also persist for many hours over their source area at equatorial latitudes, but their extended part moving poleward through low/middle latitudes have shorter duration (minutes to 1–2 hr) varying for different locations along their transportation way. The transportation pattern of the streamed plasma density depletion across North America midlatitudes is difficult to predict. There can be some dependence on the EPBs source localization—if the storm-induced EPBs developed over the Atlantic Ocean and eastern South America, there is more chance to observe and trace the streamed plasma depletions (if they occur) over the continental North America; in the cases if the storm-induced EPBs developed only over the western South America and streamed plasma depletions would

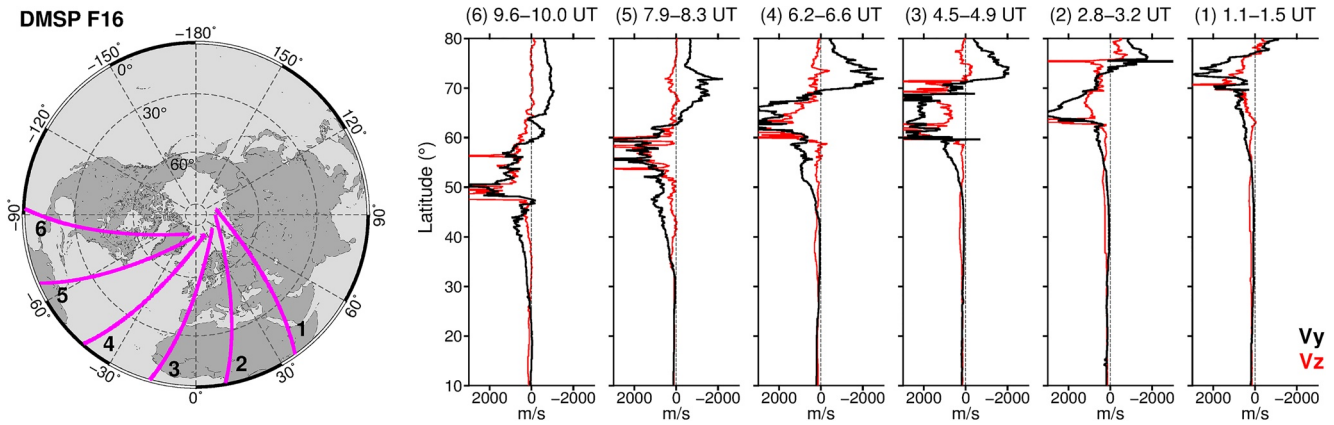

Figure 9. Defense Meteorological Satellite Program F16 observations of ion drifts along several night-time orbits in the Northern Hemisphere during 01–10 UT on 26 August 2018. Black line shows variations in horizontal (cross-track) ion drift (*Vy*), red line–vertical ion drift (*Vz*). Positive velocity values show westward direction for *Vy* and upward for *Vz*.

occur and move in the northwestward direction, we have a rather limited coverage by the ground-based GNSS stations, mainly western coast of North America and then a data gap in the Pacific, to detect its further evolution. The physical mechanisms of such streamed plasma depletions remain unclear. It is supposed that they can occur for geomagnetic storms under some particular combination of steady southward IMF, Sub Auroral Polarization Stream (SAPS) electric fields, and enhanced westward drifts at midlatitudes, resulting in northwestward plasma transportation equatorward of the SAPS region. There are multiple other factors to account for such as time of local sunset, time and intensity of penetrating electric fields, ambient plasma density etc. We should also highlight a prominent similarity in the northwestward transportation path between the observed streamed plasma density depletions and storm-enhanced-density (SED) plumes that can be observed in the same North America region during geomagnetic disturbances. The poleward transportation of the SED plumes from low latitudes toward auroral region is usually attributed to a strong convection and SAPS electric fields (Foster & Rideout, 2007). In the recent paper of Huang (2020), it was investigated importance of storm-induced westward drifts on plasma transportation in the equatorial ionosphere and a new mechanism was proposed to explain how SAPS-associated electric fields can penetrate the equatorial ionosphere, causing enhanced westward drifts here and at midlatitudes. Such type of westward drift may also play a key role in transportation of plasma irregularities from extended EPBs toward midlatitudes that we found in the North America sector.

On Figure 9, we presented variations of ion drifts along six consecutive night-time orbits of the DMSP F16 in the Northern Hemisphere during 01–10 UT on 26 August 2018. We observed very strong westward plasma drifts (*Vy*) exceeding 2,000 m/s along all these orbits from the European to American sectors. With each orbit, the zone of westward drifts moved further equatorward from ~72°N (68° MLAT) down to ~50°N (58° MLAT) since the MIT moved rapidly equatorward during the main phase and period of the steady southward IMF. At the equatorward edge of strong westward plasma drifts, the large upward velocities were also registered ($Vz > 1{,}000$–$2{,}000$ m/s) indicating an enhanced ion upflow at the same region. Such ion drift behavior confirms the presence of the westward plasma flows that can be associated with the SAPS development, sub-auroral convection enhancement and its expansion toward lower latitudes. The SuperDARN observations also registered the strong sub-auroral westward convection with the flow velocities exceeding 800–1,000 m/s in the dusk-night sector of the Northern Hemisphere during 01–04 UT on 26 August 2018 (not shown here; http://vt.superdarn.org/). Thus, strong westward plasma drifts were registered prior an occurrence of the plasma density irregularities streamed in the northwestward direction in North America.

Therefore, geomagnetic storms during low solar activity can trigger formation of extreme EPBs with unpredicted extent, capable to affect low and middle latitudes. The unexpected development of ionospheric irregularities can be dangerous for the normal operation of GNSS and other systems used trans-ionospheric radio waves propagation links. In particular, the ionospheric plasma irregularities with similar intensity developed at low and middle latitudes during strong geomagnetic storms in 2015 and 2017 (when solar activity was higher than that of August 2018) have impacted the GNSS-based positioning performance for the ground-based stations and even for low

earth orbit kinematic orbit (Yang et al., 2020; Zakharenkova & Cherniak, 2021). Occurrence of the ionospheric irregularities of equatorial origin at midlatitudes is unpredictable and non-well-understood phenomenon that requires more observational and simulation studies.

Data Availability Statement

The authors acknowledge ESA for Swarm data (http://earth.esa.int/swarm), NGDC NOAA for DMSP data (https://satdat.ngdc.noaa.gov/dmsp/data/), and NASA/GSFC's Space Physics Data Facility's OMNIWeb service for geophysical parameters data (https://omniweb.gsfc.nasa.gov). AE index was provided by WDC for Geomagnetism, Kyoto (http://wdc.kugi.kyoto-u.ac.jp/ae_realtime/201808/index.html; World Data Center for Geomagnetism, Kyoto et al., 2015); Kp index was provided by GFZ Potsdam (Matzka et al., 2021). Jason-2/3 altimeter observations are available through NASA PO.DAAC portal (https://podaac-tools.jpl.nasa.gov/drive/files/allData/). Jason-2/3 GPS observations are available through NOAA CLASS portal (https://www.avl.class.noaa.gov/saa/products/catSearch). GNSS data are available with UNAVCO (https://data.unavco.org/archive/gnss/rinex/obs/), CORS (https://geodesy.noaa.gov/corsdata), IGS (https://igs.org/data/#daily_data), SmartNetNA (www.smartnetna.com), Natural Resources Canada (webapp.geod.nrcan.gc.ca), CHAIN (Jayachandran et al., 2009), SOPAC (http://garner.ucsd.edu), RBMC Brazil (https://www.ibge.gov.br/en/geosciences/methods-and-reference-documents/other-technical-documents/19213-brazilian-network-for-continuous-monitoring-of-the-gnss-systems.html?=&t=downloads), RAMSAC CORS NGI Argentina (Piñón et al., 2018). Raw ionograms from DIDBase digisonde network are available through GIRO (http://giro.uml.edu/; Reinisch & Galkin, 2011), plotted using SAO Explorer. This paper uses ionospheric data from USAF NEXION Digisonde network, NEXION Program Manager is Mark Leahy.

Acknowledgments
The research is supported by NASA LWS (Grant NNX15AB83G) and National Science Centre, Poland (Grant 2017/27/B/ST10/02190).

References

Aa, E., Huang, W., Liu, S., Ridley, A., Zou, S., Shi, L., & Wang, T. (2018). Midlatitude plasma bubbles over China and adjacent areas during a magnetic storm on 8 September 2017. *Space Weather*, *16*(3), 321–331. https://doi.org/10.1002/2017SW001776

Aa, E., Zou, S., Ridley, A., Zhang, S., Coster, A. J., Erickson, P. J., & Ren, J. (2019). Merging of storm time midlatitude traveling ionospheric disturbances and equatorial plasma bubbles. *Space Weather*, *17*(2), 285–298. https://doi.org/10.1029/2018SW002101

Abdu, M. A. (2012). Equatorial spread F/plasma bubble irregularities under storm time disturbance electric fields. *Journal of Atmospheric and Solar-Terrestrial Physics*, *75–76*, 44–56. https://doi.org/10.1016/j.jastp.2011.04.024

Akasofu, S. I. (1966). The auroral oval, the auroral substorm, and their relations with the internal structure of the magnetosphere. *Planetary and Space Science*, *14*(5), 587–595.

Astafyeva, E., Bagiya, M. S., Förster, M., & Nishitani, N. (2020). Unprecedented hemispheric asymmetries during a surprise ionospheric storm: A game of drivers. *Journal of Geophysical Research: Space Physics*, *125*(3), e2019JA027261. https://doi.org/10.1029/2019JA027261

Basu, S., Basu, S., Groves, K. M., Mackenzie, E., Keskinen, M. J., & Rich, F. J. (2005). Near-simultaneous plasma structuring in the midlatitude and equatorial ionosphere during magnetic superstorms. *Geophysical Research Letters*, *32*, L12S05. https://doi.org/10.1029/2004GL021678

Basu, S., Basu, S., Rich, F. J., Groves, K. M., MacKenzie, E., Coker, C., et al. (2007). Response of the equatorial ionosphere at dusk to penetration electric fields during intense magnetic storms. *Journal of Geophysical Research*, *112*, A08308. https://doi.org/10.1029/2006JA012192

Basu, S., Basu, S., Valladares, C. E., Yeh, H. C., Su, S. Y., MacKenzie, E., & Bullett, T. W. (2001). Ionospheric effects of major magnetic storms during the international space weather period of September and October 1999: GPS observations, VHF/UHF scintillations, and in situ density structures at middle and equatorial latitudes. *Journal of Geophysical Research*, *106*(A12), 30389–30413. https://doi.org/10.1029/2001ja001116

Bhattacharyya, A., Basu, S., Groves, K. M., Valladares, C. E., & Sheehan, R. (2002). Effect of magnetic activity on the dynamics of equatorial F region irregularities. *Journal of Geophysical Research*, *107*(A12), 1–7. https://doi.org/10.1029/2002JA009644

Blanc, M., & Richmond, A. D. (1980). The ionospheric disturbance dynamo. *Journal of Geophysical Research*, *85*(A4), 1669. https://doi.org/10.1029/ja085ia04p01669

Carter, B. A., Yizengaw, E., Pradipta, R., Retterer, J. M., Groves, K., Valladares, C., et al. (2016). Global equatorial plasma bubble occurrence during the 2015 St. Patrick's Day storm. *Journal of Geophysical Research: Space Physics*, *121*(1), 894–905. https://doi.org/10.1002/2015JA022194

Cherniak, I., Krankowski, A., & Zakharenkova, I. (2018). ROTI maps: A new IGS ionospheric product characterizing the ionospheric irregularities occurrence. *GPS Solutions*, *22*(3). https://doi.org/10.1007/s10291-018-0730-1

Cherniak, I., & Zakharenkova, I. (2016). First observations of super plasma bubbles in Europe. *Geophysical Research Letters*, *43*(21), 11137–11145. https://doi.org/10.1002/2016GL071421

Cherniak, I., & Zakharenkova, I. (2019). Evaluation of the IRI-2016 and NeQuick electron content specification by COSMIC GPS radio occultation, ground-based GPS and Jason-2 joint altimeter/GPS observations. *Advances in Space Research*, *63*(6), 1845–1859. https://doi.org/10.1016/j.asr.2018.10.036

Cherniak, I., Zakharenkova, I., & Redmon, R. J. (2015). Dynamics of the high-latitude ionospheric irregularities during the 17 March 2015 St. Patrick's Day storm: Ground-based GPS measurements. *Space Weather*, *13*(9), 585–597. https://doi.org/10.1002/2015SW001237

Cherniak, I., Zakharenkova, I., & Sokolovsky, S. (2019). Multi-instrumental observation of storm-induced ionospheric plasma bubbles at equatorial and middle latitudes. *Journal of Geophysical Research: Space Physics*, *124*(3), 1491–1508. https://doi.org/10.1029/2018JA026309

Doherty, P., Coster, A. J., & Murtagh, W. (2004). Eye on the ionosphere: Space weather effects of October–November 2003. *GPS Solutions*, *8*(4), 267–271. https://doi.org/10.1007/s10291-004-0109-3

Fejer, B. G. (1991). Low latitude electrodynamic plasma drifts: A review. *Journal of Atmospheric and Terrestrial Physics*, *53*(8), 677–693. https://doi.org/10.1016/0021-9169(91)90121-M

Fejer, B. G., Jensen, J. W., & Su, S.-Y. (2008). Seasonal and longitudinal dependence of equatorial disturbance vertical plasma drifts. *Geophysical Research Letters*, *35*(20), L20106. https://doi.org/10.1029/2008GL035584

Fejer, B. G., Scherliess, L., & de Paula, E. R. (1999). Effects of the vertical plasma drift velocity on the generation and evolution of equatorial spread F. *Journal of Geophysical Research*, *104*(A9), 19859–19869. https://doi.org/10.1029/1999ja900271

Foster, J. C., & Rich, F. J. (1998). Prompt midlatitude electric field effects during severe geomagnetic storms. *Journal of Geophysical Research*, *103*(A11), 26367–26372.

Foster, J. C., & Rideout, W. (2007). Storm enhanced density: Magnetic conjugacy effects. *Annales Geophysicae*, *25*(8), 1791–1799. https://doi.org/10.5194/angeo-25-1791-2007

Fuller-Rowell, T. J., Millward, G. H., Richmond, A. D., & Codrescu, M. V. (2002). Storm-time changes in the upper atmosphere at low latitudes. *Journal of Atmospheric and Solar-Terrestrial Physics*, *64*(12), 1383–1391. https://doi.org/10.1016/S1364-6826(02)00101-3

Greenspan, M. E., Rasmussen, C. E., Burke, W. J., & Abdu, M. A. (1991). Equatorial density depletions observed at 840 km during the great magnetic storm of March 1989. *Journal of Geophysical Research*, *96*(A8), 13931–13942.

Hosokawa, K., & Nishitani, N. (2010). Plasma irregularities in the duskside subauroral ionosphere as observed with midlatitude SuperDARN radar in Hokkaido, Japan. *Radio Science*, *45*(4), RS4003. https://doi.org/10.1029/2009rs004244

Huang, C. S. (2020). Westward plasma drifts in the nighttime equatorial ionosphere during severe magnetic storms: A new type of penetration electric fields caused by subauroral polarization Stream. *Journal of Geophysical Research: Space Physics*, *125*(10), e2020JA028300. https://doi.org/10.1029/2020JA028300

Huang, C. S., Foster, J. C., & Kelley, M. C. (2005). Long-duration penetration of the interplanetary electric field to the low-latitude ionosphere during the main phase of magnetic storms. *Journal of Geophysical Research*, *110*(A11), 1–13. https://doi.org/10.1029/2005JA011202

Huang, C. S., Foster, J. C., & Sahai, Y. (2007). Significant depletions of the ionospheric plasma density at middle latitudes: A possible signature of equatorial spread F bubbles near the plasmapause. *Journal of Geophysical Research*, *112*(A5), A05315. https://doi.org/10.1029/2007JA012307

Hysell, D. L., & Burcham, J. D. (2002). Long term studies of equatorial spread F using the JULIA radar at Jicamarca. *Journal of Atmospheric and Solar-Terrestrial Physics*, *64*(12–14), 1531–1543. https://doi.org/10.1016/S1364-6826(02)00091-3

Iyemori, T. (1990). Storm-time magnetospheric currents inferred from mid-latitude geomagnetic field variations. *Journal of Geomagnetism and Geoelectricity*, *42*(11), 1249–1265. https://doi.org/10.5636/jgg.42.1249

Iyemori, T., & Rao, D. R. K. (1996). Decay of the Dst field of geomagnetic disturbance after substorm onset and its implication to storm-substorm relation. *Annales Geophysicae*, *14*, 608–618. https://doi.org/10.1007/s00585-996-0608-3

Jakowski, N., Mielich, J., Borries, C., Cander, L., Krankowski, A., Nava, B., & Stankov, S. M. M. (2008). Large-scale ionospheric gradients over Europe observed in October 2003. *Journal of Atmospheric and Solar-Terrestrial Physics*, *70*(15), 1894–1903. https://doi.org/10.1016/j.jastp.2008.03.020

Jayachandran, P. T., Langley, R. B., MacDougall, J. W., Mushini, S. C., Pokhotelov, D., Hamza, A. M., et al. (2009). Canadian high Arctic ionospheric network (CHAIN). *Radio Science*, *44*, RS0A03. https://doi.org/10.1029/2008RS004046

Joshi, D., Groves, K., & Retterer, J. (2021). The dependence of the irregularity parameter characterizing the equatorial ionospheric irregularities on the background ionospheric density. *Journal of Nepal Paediatric Society*, *7*(1), 1–5. https://doi.org/10.3126/jnphyssoc.v7i1.36967

Kauristie, K., Weygand, J., Pulkkinen, T. I., Murphree, J. S., & Newell, P. T. (1999). Size of the auroral oval: UV ovals and precipitation boundaries compared. *Journal of Geophysical Research*, *104*, 2321–2331.

Keskinen, M. J., & Ossakow, S. L. (1983). Theories of high-latitude ionospheric irregularities: A review. *Radio Science*, *18*(6), 1077–1091. https://doi.org/10.1029/RS018i006p01077

Kikuchi, T., Hashimoto, K. K., & Nozaki, K. (2008). Penetration of magnetospheric electric fields to the equator during a geomagnetic storm. *Journal of Geophysical Research*, *113*(6), 1–10. https://doi.org/10.1029/2007JA012628

Kil, H., Lee, W. K., Paxton, L. J., Hairston, M. R., & Jee, G. (2016). Equatorial broad plasma depletions associated with the evening prereversal enhancement and plasma bubbles during the 17 March 2015 storm. *Journal of Geophysical Research: Space Physics*, *121*(10), 10209–10219. https://doi.org/10.1002/2016JA023335

Li, G., Ning, B., Wang, C., Abdu, M. A., Otsuka, Y., Yamamoto, M., & Chen, J. (2018). Storm-enhanced development of postsunset equatorial plasma bubbles around the Meridian 120°E/60°W on 7–8 September 2017. *Journal of Geophysical Research: Space Physics*, *123*(9), 7985–7998. https://doi.org/10.1029/2018JA025871

Lissa, D., Srinivasu, V. K. D., Prasad, D. S. V. V. D., & Niranjan, K. (2020). Ionospheric response to the 26 August 2018 geomagnetic storm using GPS-TEC observations along 80°E and 120°E longitudes in the Asian sector. *Advances in Space Research*, *66*(6), 1427–1440. https://doi.org/10.1016/j.asr.2020.05.025

Lühr, H., Park, J., Gjerloev, J. W., Rauberg, J., Michaelis, I., Merayo, J. M. G., & Brauer, P. (2015). Field-aligned currents' scale analysis performed with the Swarm constellation. *Geophysical Research Letters*, *42*(1), 1–8. https://doi.org/10.1002/2014GL062453

Ma, G., & Maruyama, T. (2006). A super bubble detected by dense GPS network at east Asian longitudes. *Geophysical Research Letters*, *33*(21), L21103. https://doi.org/10.1029/2006GL027512

Mannucci, A. J., Tsurutani, B. T., Iijima, B. A., Komjathy, A., Saito, A., Gonzalez, W. D., & Skoug, R. (2005). Dayside global ionospheric response to the major interplanetary events of October 29-30, 2003 "Halloween Storms". *Geophysical Research Letters*, *32*(12), 1–4. https://doi.org/10.1029/2004GL021467

Mansilla, G. A., & Zossi, M. M. (2020). Longitudinal variation of the ionospheric response to the 26 August 2018 geomagnetic storm at equatorial/low latitudes. *Pure and Applied Geophysics*, *177*(12), 5833–5844. https://doi.org/10.1007/s00024-020-02601-1

Martinis, C., Baumgardner, J., Mendillo, M., Wroten, J., Coster, A., & Paxton, L. (2015). The night when the auroral and equatorial ionospheres converged. *Journal of Geophysical Research: Space Physics*, *120*, 8085–8095. https://doi.org/10.1002/2015JA021555

Matzka, J., Bronkalla, O., Tornow, K., Elger, K., & Stolle, C. (2021). *Geomagnetic Kp index. V. 1.0*. GFZ Data Services. https://doi.org/10.5880/Kp.0001

Mrak, S., Semeter, J., Nishimura, Y., Rodrigues, F. S., Coster, A. J., & Groves, K. (2020). Leveraging geodetic GPS receivers for ionospheric scintillation science. *Radio Science*, *55*(11), e2020RS007131. https://doi.org/10.1029/2020RS007131

Nishitani, N., Ruohoniemi, J. M., Lester, M., Baker, J. B. H., Koustov, A. V., Shepherd, S. G., & Kikuchi, T. (2019). Review of the accomplishments of mid-latitude super dual auroral radar network (SuperDARN) HF radars. *Progress in Earth and Planetary Science*, *6*(1). https://doi.org/10.1186/s40645-019-0300-3

Pi, X., Mannucci, A. J., Lindqwister, U. J., & Ho, C. M. (1997). Monitoring of global ionospheric irregularities using the worldwide GPS network. *Geophysical Research Letters*, *24*(18), 2283–2286. https://doi.org/10.1029/97GL02273

Piñón, D. A., Gómez, D. D., Smalley, R., Cimbaro, S. R., Lauría, E. A., & Bevis, M. G. (2018). The history, state, and future of the Argentine continuous satellite monitoring network and its contributions to geodesy in Latin America. *Seismological Research Letters*, *89*(2A), 475–482. https://doi.org/10.1785/0220170162

Reinisch, B. W., & Galkin, I. A. (2011). Global ionospheric radio observatory (GIRO). *Earth Planets and Space*, *63*, 377–381. https://doi.org/10.5047/eps.2011.03.001

Retterer, J. M., & Gentile, L. C. (2009). Modeling the climatology of equatorial plasma bubbles observed by DMSP. *Radio Science*, *44*(5). https://doi.org/10.1029/2008RS004057

Ruohoniemi, J. M., Greenwald, R. A., Villain, J.-P., Baker, K. B., Newell, P. T., & Meng, C.-I. (1988). Coherent HF radar backscatter from small-scale irregularities in the dusk sector of the subauroral ionosphere. *Journal of Geophysical Research*, *93*(A11), 12871–12882. https://doi.org/10.1029/ja093ia11p12871

Scherliess, L., & Fejer, B. G. (1997). Storm time dependence of equatorial disturbance dynamo zonal electric fields. *Journal of Geophysical Research*, *102*(A12), 24037–24046.

Sori, T., Shinbori, A., Otsuka, Y., Tsugawa, T., & Nishioka, M. (2021). The occurrence feature of plasma bubbles in the equatorial to midlatitude ionosphere during geomagnetic storms using long-term GNSS-TEC data. *Journal of Geophysical Research: Space Physics*, *126*(5), e2020JA029010. https://doi.org/10.1029/2020ja029010

Spogli, L., Sabbagh, D., Regi, M., Cesaroni, C., Perrone, L., Alfonsi, L., & Ippolito, A. (2021). Ionospheric response over Brazil to the August 2018 geomagnetic storm as probed by CSES-01 and Swarm satellites and by local ground-based observations. *Journal of Geophysical Research: Space Physics*, *126*(2), e2020JA028368. https://doi.org/10.1029/2020JA028368

Stolle, C., Kervalishvili, G., & Rauberg, J. (2017). *Swarm L2 FAC-dual product description*. (Tech. Rep. SW-TR-GFZ-GS-008). GFZ.

Sultan, P. J. (1996). Linear theory and modeling of the Rayleigh-Taylor instability leading to the occurrence of equatorial spread F. *Journal of Geophysical Research*, *101*(A12), 26875–26891. doi.org/10.1029/96JA00682

Tsunoda, R. T. (1988). High-latitude F region irregularities: A review and synthesis. *Reviews of Geophysics*, *26*(4), 719–760. https://doi.org/10.1029/RG026i004p00719

Tsurutani, B., Mannucci, A., Iijima, B., Abdu, M. A., Sobral, J. H. A., Gonzalez, W., & Vasyliunas, V. M. (2004). Global dayside ionospheric uplift and enhancement associated with interplanetary electric fields. *Journal of Geophysical Research*, *109*(A8), 1–16. https://doi.org/10.1029/2003JA010342

Tsurutani, B. T., Verkhoglyadova, O. P., Mannucci, A. J., Saito, A., Araki, T., Yumoto, K., & Vasyliunas, V. M. (2008). Prompt penetration electric fields (PPEFs) and their ionospheric effects during the great magnetic storm of 30-31 October 2003. *Journal of Geophysical Research*, *113*(5), 1–10. https://doi.org/10.1029/2007JA012879

Tulasi Ram, S., Rama Rao, P. V. S., Prasad, D. S. V. V. D., Niranjan, K., Gopi Krishna, S., Sridharan, R., & Ravindran, S. (2008). Local time dependent response of postsunset ESF during geomagnetic storms. *Journal of Geophysical Research*, *113*(A7), A07310. https://doi.org/10.1029/2007JA012922

World Data Center for Geomagnetism, Kyoto, Nose, M., Iyemori, T., Sugiura, M., & Kamei, T. (2015). *Geomagnetic AE index*. https://doi.org/10.17593/15031-54800

Xiong, C., Park, J., Lühr, H., Stolle, C., & Ma, S. Y. (2010). Comparing plasma bubble occurrence rates at CHAMP and GRACE altitudes during high and low solar activity. *Annales Geophysicae*, *28*(9), 1647–1658. https://doi.org/10.5194/angeo-28-1647-2010

Yang, Z., Morton, Y. T. J., Zakharenkova, I., Cherniak, I., Song, S., & Li, W. (2020). Global view of ionospheric disturbance impacts on kinematic GPS positioning solutions during the 2015 St. Patrick's day storm. *Journal of Geophysical Research: Space Physics*, *125*, e2019JA027681. https://doi.org/10.1029/2019JA027681

Yeh, H. C., Su, S.-Y., & Heelis, R. A. (2001). Storm time plasma irregularities in the pre-dawn hours observed by the low-latitude ROCSAT-1 satellite at 600 Km. *Geophysical Research Letters*, *28*(4), 685–688. https://doi.org/10.1029/2000GL012183

Younas, W., Amory-Mazaudier, C., Khan, M., & Fleury, R. (2020). Ionospheric and magnetic signatures of a space weather event on 25–29 August 2018: CME and HSSWs. *Journal of Geophysical Research: Space Physics*, *125*(8), 1–18. https://doi.org/10.1029/2020JA027981

Zakharenkova, I., Astafyeva, E., & Cherniak, I. (2015). Early morning irregularities detected with spaceborne GPS measurements in the topside ionosphere: A multisatellite case study. *Journal of Geophysical Research: Space Physics*, *120*(10), 8817–8834. https://doi.org/10.1002/2015JA021447

Zakharenkova, I., & Cherniak, I. (2020). When plasma streams tie up equatorial plasma irregularities with auroral ones. *Space Weather*, *18*(2), e2019SW002375. https://doi.org/10.1029/2019SW002375

Zakharenkova, I., & Cherniak, I. (2021). Effects of storm-induced equatorial plasma bubbles on GPS-based kinematic positioning at equatorial and middle latitudes during the September 7–8, 2017, geomagnetic storm. *GPS Solutions*, *25*(4). https://doi.org/10.1007/s10291-021-01166-3

Zakharenkova, I., Cherniak, I., & Krankowski, A. (2019). Features of storm-induced ionospheric irregularities from ground-based and spaceborne GPS observations during the 2015 St. Patrick's day storm. *Journal of Geophysical Research: Space Physics*, *124*(12), 10728–10748. https://doi.org/10.1029/2019JA026782